Catalysis Science & Technology

Accepted Manuscript

ROYAL SOCIETY OF CHEMISTRY

www.rsc.org/catalysis

Improved O_2 Evolution from Water Splitting Reaction over Tetragonal $BiVO_4$ by Er^{3+}, Y^{3+} Co-doping

By Sergio Obregón and Gerardo Colón

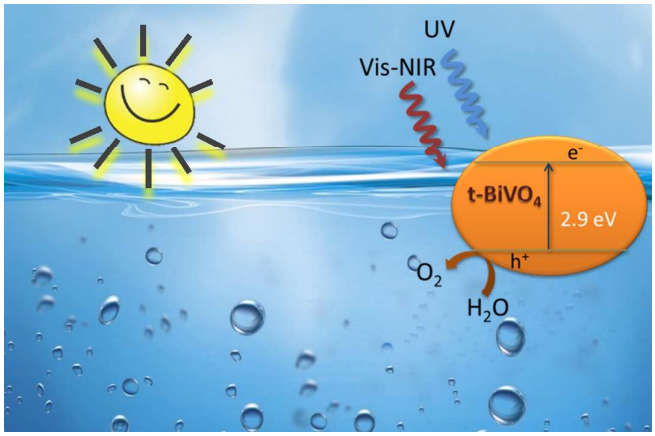

Improved O_2 Evolution from Water Splitting Reaction over Tetragonal $BiVO_4$ by Er^{3+}, Y^{3+} Co-doping

S. Obregón and G. Colón†

Instituto de Ciencia de Materiales de Sevilla. Centro Mixto CSIC-Universidad de Sevilla. C/ Américo Vespucio, 49. 41092 Sevilla. Spain

† *Corresponding author*: gcolon@icmse.csic.es *Tel. + 34 954489536.*

Abstract

Erbium-Yttrium co-doped $BiVO_4$ with tetragonal structure are synthesized by means of a surfactant free hydrothermal method. The studied photocatalysts show good photoactivities under sun-like excitation for the degradation of *Methylene Blue* and O_2 evolution reactions. From the structural and morphological characterization it has been stated that the presence of lanthanides induces the stabilization of the tetragonal phase probably due to the substitutionally incorporation in the $BiVO_4$ lattice. The photocatalytic performance under visible-NIR clearly evidences the occurrence of an up-conversion process involved in the overall photo-electronic mechanism. Tetragonal phase $Er_{0.0075},Y_{0.03}$-$Bi_{0.9625}VO_4$ system gives the highest O_2 evolution rate (425 $\mu mol \cdot g^{-1} \cdot h^{-1}$) under sun-like excitation, being 8 times higher than that attained for m-$BiVO_4$ (53 $\mu mol \cdot g^{-1} \cdot h^{-1}$).

Keyword: erbium; yttrium; $BiVO_4$; tetragonal; photocatalysis; O_2 evolution.

Introduction.

Nowadays, the recent socioeconomic demands concerning energy and environmental pollution lead to the progress of new green technologies such as photocatalysis.[1,2] Within this frame, in the last years heterogeneous photocatalysis has focused its attention to the development of novel alternative materials to traditional TiO_2 capable to use of sunlight as the green energy source.[3,4] Since the discovery of the photocatalytic water cleavage plenty of efforts have been paid to develop new photocatalyst for overall water splitting, and some excellent results were obtained.[5,6] Nevertheless, the efficiencies achieved are still far from practical applications. A typical approach to accomplish overall water splitting is designing a two coupled photoreaction that is called Z-scheme system.[7,8] While H_2 production from aqueous solution containing sacrificial reagents has been demonstrated to be a quite efficient process, the O_2 production semireaction still remains a challenging redox process.[9] Hence, synthesis of highly active photocatalyst for O_2 evolution reaction turns up quite important for enhancing the efficiency of solar-hydrogen conversion. In this sense, it has been stated that $BiVO_4$ is one of the most active system for this reaction.[10,11] This is due to its relatively low band gap (2.4 eV for monoclinic $BiVO_4$) and the adequate position of valence and conduction bands as compared to the redox potential for water oxidation. As it is widely known, the photocatalytic properties of $BiVO_4$ are strongly dependent on its morphology and microstructure.[12,13,14] Among the three main crystalline phases described (monoclinic scheelite, tetragonal zircon, and tetragonal scheelite), the monoclinic one appears as the only one showing high photoactivity for O_2 evolution reaction under visible-light irradiation.[15,16,17] This is due to the particular structure of the valence band (which is formed by Bi *6s* or a hybrid orbital of Bi *6s* and O *2p*) and the

conduction band (formed by V *3d*). This band configuration is the responsible of its narrow band gap (ca. 2.4 eV) compared to 3.0 eV exhibited by the tetragonal one.

A novel challenging approach followed in order to use as efficient as possible the solar light would consist on the assembly of a photocatalyst with a luminescence material.[18,19,20,21] Within this configuration we have recently described the assembly of TiO_2 with Er^{3+} acting as up-converting doping cation.[22] From those results, we proposed that the presence of Er^{3+} doping into TiO_2 as host matrix favors a double mechanism, under *UV* and *vis-NIR* excitation. We have also stated that Er^{3+}-doping on $BiVO_4$ clearly stabilizes the tetragonal structure.[23] In this sense, a tentative cooperative mechanism has been proposed. The tetragonal phase stabilization has been also achieved by yttrium doping.[24] The occurrence of a heterostructured $BiVO_4$ formed by tetragonal and monoclinic phase mixture has been demonstrated to have a clear beneficial effect on the final photoactivity of the system. Fan *et al* reported that the particular m-t heterostructured $BiVO_4$ is expected to promote the separation of photoinduced electron-hole pairs.[25] These results clearly show that the behaviour of photoinduced charges is markedly dependent on the $BiVO_4$ crystalline phases. Moreover, the presence of interface in monoclinic/tetragonal heterophase provides a spatial condition for charge transfer which favours the separation of photoinduced electron-hole pairs, and changes the migration direction of photoinduced carriers.

In the present paper, we describe the substantial improvement obtained by Er,Y co-doping for O_2 evolution reaction. The combination of these two lanthanides ions with specific incidence over the structural and electronic features of the photocatalyst clearly affects the final photocatalytic activity. The correlation between different structural and electronic techniques with the photoactivities under different irradiation conditions would provide a possible explanation about the role of this co-doping.

2. Experimental.

2.1 Samples preparation

The $BiVO_4$ samples were prepared by a surfactant free hydrothermal method. First, 5 mmol of $Bi(NO_3)_3 \cdot 5H_2O$ (Sigma-Aldrich, ≥98.0%) and the stoichiometric amount of $Er(NO_3)_3$ (0.75 at%) were dissolved in 10 mL of glacial acetic acid at room temperature. A second aqueous solution was prepared by dissolving the corresponding stoichiometric amount of NH_4VO_3 (Sigma-Aldrich, ≥99.0%) or $Y(NO_3)_3$ (3.0 at%) in 60 mL of hot distilled water. Afterwards, the ammonium metavanadate solution was added to the erbium-bismuth nitrate aqueous solution and the process was accompanied with a vigorous stirring. The pH of the obtained suspension was adjusted to 9.0 by adding concentrated NH_4OH (13 $mol \cdot L^{-1}$). The slurry was encased in a Teflon vessel and heated at 140 ºC during 20 hours. The obtained precipitate was then cooled until room temperature, filtered and repeatedly washed and dried overnight at 120 °C. Afterwards, thus obtained samples were submitted to a further calcination treatment at 300 ºC for 2 h.

Tetragonal $BiVO_4$ (t-$BiVO_4$) has been also prepared as reference material. In this case we have followed a similar procedure as for m-$BiVO_4$ but using triethylamine as precipitating agent.

2.2 *Materials characterization*

BET surface area and porosity measurements were carried out by N_2 adsorption at 77 K using a Micromeritics 2010 instrument.

The chemical composition of samples has been studied by ICP analysis using a Horiba Jobin Yvon, Ultima 2.

X-ray diffraction (XRD) patterns were obtained using a Siemens D-501 diffractometer with Ni filter and graphite monochromator. The X-ray source was Cu Kα radiation (0.15406 nm). Rietveld analyses were performed by using XPert HighScore Plus software over selected samples. The diffraction patterns were recorded from *2θ* 10º to 120º with step of 0.017º and 400 s per step. Crystallite sizes were obtained from Rietveld refinement.

The UV diffuse reflectance spectra were measured using an UV–vis spectrophotometer equipped with an integrating sphere (JASCO V-570). The reference sample used was a $BaSO_4$ coated standard pattern.

Micro-Raman measurements were performed using a LabRAM Jobin Yvon spectrometer equipped with a microscope. Laser radiation (λ = 532 and 780 nm) was used as excitation source at 5 mW. All measurements were recorded under the same conditions (4 s of integration time and 10 accumulations) using a 100x magnification objective and a 125 mm pinhole.

2.3. Photocatalytic tests

The *MB* oxidation reactions were performed using a batch reactor (150 mL) with a 200W Xenon lamp. The intensity of the incident light on the solution measured with a HD2302 photometer (Delta OHM) gives 90 $W \cdot m^{-2}$ and 500 $W \cdot m^{-2}$ for *UV* and *vis-NIR* spectral ranges, respectively. For this scope LP 471 UVA sensor with spectral response 315-400 nm and LP 471 RAD sensor (spectral response 400-1050 nm) were used. The *vis-NIR* runs were performed by using a cut-off filter (λ>420 nm) which assures the complete withdrawal of *UV* incident photons. In the oxidation tests, an air flow was employed to produce a homogenous suspension of the photocatalyst in the solution. Before each experiment, the catalysts ($1 g \cdot L^{-1}$) were settled in suspension with the

reagent mixture for 15 min. The blank experiment was performed without catalyst and no dye degradation was observed after 2 hours. The evolution of the initial *MB* (ca. 10 ppm) concentration was followed through the evolution of the characteristic 664 nm band, using a centrifuged aliquot ca. 2 mL of the suspension (microcentrifuge Minispin, Eppendorf). The pH of the suspension was unchanged during the photodegradation tests (pH~6.5) for all $BiVO_4$ samples. Reaction rates were calculated assuming a first order kinetic.

The photocatalytic activities of the samples were also evaluated for the photocatalytic oxygen evolution reaction from water in an $AgNO_3$ aqueous solution (0.02 M). The reaction media was continuously thermostated at 23º-25ºC to prevent any significant effect of temperature. The catalyst suspension (1 $g \cdot L^{-1}$) was firstly degassed with a N_2 stream (150 $mL \cdot min^{-1}$) for 30 min. After that the N_2 flow was settled at 15 $mL \cdot min^{-1}$ and stabilised for 15 min. This nitrogen flow was used to displace the oxygen produced from the photoreactor headspace towards the GC measuring system. Then, the lamp (200 W Hg-Xe lamp, Oriel Instruments) was switched on and the effluent gases were analysed to quantify O_2 production by gas chromatography (Agilent 490 micro GC) using a thermal conductivity detector connected to a Molsieve 5 A and Pora-PLOT Q columns.

3. Results and discussion.

The XRD pattern shown in **Figure 1** depicts the evolution of the crystalline phase upon the incorporation of different dopant ions. As it can be observed the original monoclinic structure (PDF 75-1866) exhibited by bare $BiVO_4$ is progressively lost as Er^{3+} and Y^{3+} are incorporated. The tetragonal phase (PDF 14-0133) stabilization is more pronounced when Y^{3+} is present. This marked stabilization is related to the higher

doping level by yttrium with respect to erbium. Finally when both lanthanides are present only tetragonal phase appears. For comparison we have prepared a tetragonal reference sample, which exhibits a small fraction of monoclinic phase.

The structural features of the studied samples are summarized in **Table 1**. In the case of single doping, a clear tetragonal stabilization is observed. By observing the monoclinic and tetragonal cell volumes, it arises that the incorporation of dopant appears quite different. Thus, while the monoclinic unit cell experiments a slight increase as lanthanides are incorporated, for the tetragonal one a slight reduction in the cell volume is attained. This behavior would indicate a rather different location of the dopant in each $BiVO_4$ structure. Thus, for monoclinic structure Ln^{3+} would be placed in the interstitial sites. The calculated microstrain would evidence a more stressed structure, especially when yttrium is incorporated. On the other hand, the tetragonal structure would accommodate the dopant ions substitutionally in Bi^{3+} sites since cell volumes tend to diminish. This fact would be supported by considering the ionic radii of dopants (89 pm and 104 pm for Er^{3+} and Y^{3+} respectively) with respect to Bi^{3+} (117 pm).[26] This cell contraction would also provoke a structural stress giving higher microstrain with respect to undoped t-$BiVO_4$. In accordance to this behavior, the co-doped system also denotes the effect. The pure tetragonal structure shows a significantly lower cell volume which would indicate the substitutionally occupation of the lanthanides ions.

Raman spectroscopy is an effective tool for the structural characterization of materials. In **Figure 2** we show the Raman spectra for the studied samples registered upon green laser excitation. The monoclinic $BiVO_4$ Raman spectrum is characterized by the presence of typical bands at 210, 324, 366, 640, 710 and 825 cm^{-1}.[27] These two latter bands are associated to stretching modes corresponding to the V-O bond and provide

valuable structural information.[28] For lanthanide doped samples, it can be noticed the monoclinic to tetragonal transition by the ν_s (V-O) band shift from 820 cm^{-1} to 850 cm^{-1} and the disappearance of the δ (VO_4^{3-}) doublet of the monoclinic phase (**Figure 2.a**). As it has been previously reported, Raman spectra containing rare earth ions are strongly affected by the luminescence emission. Thus, Er^{3+}-containing samples exhibit noticeable luminescence emission bands (**Figure 2.b**). It is worthy to note that this luminescence bands appear highly intense for co-doped $BiVO_4$ with respect to Er^{3+}-$BiVO_4$. This would indicate that the presence of yttrium would exalt to a certain extent the luminescence properties of erbium. This fact has been previously reported for Er^{3+}-Y^{3+} co-doped TiO_2.[29] Thus, Ting *et al* argued that the distorted local structure of Er^{3+} ions due to yttrium presence could increase the probability of the normally forbidden intra-4f transition and improve the photoluminescence process. In order to examine the structural evolution of $BiVO_4$ samples without the interference of erbium luminescence emission, we have performed the Raman spectra by red laser excitation (**Figure 3**). From these spectra the monoclinic to tetragonal transition due to lanthanide doping can be clearly envisaged. Thus the ν_s(V-O) stretching mode at 825 cm^{-1} for the monoclinic structure appears with a shoulder at higher Raman shift when erbium or yttrium is incorporated. This evidently denotes the co-existence of both phases as it was stated from XRD. Moreover, the co-doped $BiVO_4$ clearly shows a single band at 850 cm^{-1} pointing out the presence of tetragonal phase exclusively. From the Raman shift position corresponding to the symmetric stretching mode it is possible to attain information about the V-O bond length in the VO_4^{3-} tetrahedron through the following expression[30]:

$$\nu(cm^{-1}) = 21349 \cdot e^{(-1.9176R(\text{Å}))}$$

In **Table 2** we present the calculated V-O bond distances (R) for bare $BiVO_4$ and doped

systems. By observing the calculated bond lengths it is worth noting that while the incorporation of erbium does not induces a significant distortion in the VO_4^{3-} tetrahedron in both monoclinic and tetragonal structure, yttrium doping induces a slight decrease in both structures.[31] This result is in accordance to the microstrain values showed in **Table 1** for Er^{3+}-$BiVO_4$ and could be correlated to the lower ionic radius of Er^{3+} with respect to Y^{3+} as well as to the lower erbium doping level. The shorter bond length in yttrium doped systems would indicate a stronger packed tetragonal structure and would affect to the lone pair distortion around the bismuth cation.[27] It has been argued that the structural distortion is directly proportional to the hole mobility.[32]

In order to study the electronic states of different studied systems UV–vis DRS spectra were performed (**Figure 4**). As can be seen from the figure, the absorption edges of doped $BiVO_4$ samples orderly varied denoting the structural changes above discussed. It can be noticed that t-$BiVO_4$ shows a small absorption in the visible range. This small contribution denotes the presence a residual m-$BiVO_4$ that has been previously detected from XRD (see **Table 1**). Even Er^{3+},Y^{3+}-$BiVO_4$ sample presents this a small shoulder in this region in spite of from Rietveld analysis and Raman spectrum the monoclinic fraction was negligible. Accordingly, the different phase compositions of $BiVO_4$ result in different band gaps (**Table 3**). As monoclinic to tetragonal transition is taking place, the band gaps tend to shift from visible region to UV light region.

Other physicochemical properties such as chemical composition and surface area of the studied systems are summarized on **Table 3**. The effectiveness of doping is supported by the chemical analysis by ICP technique. Erbium and yttrium relative content with respect to bismuth are in accordance to the nominal values. Regarding to the surface area values it can be observed that the structural changes are clearly accompanied by a certain modification in the surface area values. As it has been widely reported, the

tetragonal phase $BiVO_4$ exhibits relatively larger surface area values with respect to the monoclinic one.[23,24]

The morphology of $BiVO_4$ has been extensively reported to be dependent on the preparation route.[33] In our case, bare m-$BiVO_4$ shows a rod-like morphology (**Figure 5.a**) while t-$BiVO_4$ exhibits square-bar particles (**Figure 5.b**). As erbium or yttrium ion is incorporated, the morphology of the sample clearly denotes the mixture of the two phases present (**Figures 5.c** and **d**).[33] For erbium doping the tetragonal particles presents a clear evolution form square-bar shape toward thinner acicular morphology while monoclinic seems to evolve toward well-defined prism-like morphology. As it can be stated, the incorporation of yttrium induces a quite drastic change in morphology. The tetragonal acicular particles seem to decrease in size showing a rod-like morphology.[24] Co-doped $BiVO_4$ follows the above mentioned evolution and only small rice-like particles appears (200-500 nm length and 100 nm width) (**Figures 5.e and 5.f**).

In **Figure 6** we show the photocatalytic activity of the studied systems. The incorporation of either erbium or yttrium ion into the $BiVO_4$ structure produces a clear improvement in the photodegradation of *MB*, being Er^{3+}-$BiVO_4$ slightly more active than Y^{3+}-$BiVO_4$ (**Figure 6.a**). In both cases, the main crystalline phase was the tetragonal one, though for Er^{3+}-$BiVO_4$ the monoclinic fraction is slightly higher. The simultaneous Er^{3+},Y^{3+} doping improves the photocatalytic activity with respect to single doped systems in spite of that pure tetragonal phase is present. If we compare the calculated reaction rates of this later sample with the corresponding for m-$BiVO_4$ and t-$BiVO_4$ a dramatic enhancement is taking place (**Table 3**). For Er^{3+},Y^{3+} co-doped sample the surface area value is slightly higher than for m-$BiVO_4$, however the comparison with t-$BiVO_4$ clearly states that the controlling parameter in the photoactivity is other

than BET surface area.

In order to elucidate the specific role of erbium on the reaction mechanism, we have performed the degradation reaction under *vis-NIR* irradiation (**Figure 6.b**). As expected, m-$BiVO_4$ shows the best photocatalytic performance while t-$BiVO_4$ shows a negligible photoactivity. However, although all doped systems show a tetragonal-rich structure, the photoactivities under *visible-NIR* irradiation appear somewhat improved (**Table 3**). From this result it is clear that besides the increase of surface area values due to tetragonal phase presence in single doped $BiVO_4$ with respect to m-$BiVO_4$, the particular structural features of the systems (monoclinic-tetragonal heterostructure) might be in principle the reason of the photocatalytic activity enhancement. In this sense, as reported by Fan *et al*, the particular monoclinic-tetragonal heterostructured $BiVO_4$ is expected to promote the separation of photoinduced electron-hole pairs.[25] These authors proposed that the enhanced photoactivity would be achieved by the optimization of the electron-hole separation due to the heterostructure formation. On this basis, we could state that the conjunction of morphological and structural features clearly provides better photocatalytic performance. Moreover, erbium presence would also particularly affect to the photoelectronic mechanism under *vis-NIR* excitation which could explain the better performance with respect to Y^{3+}-$BiVO_4$.[23] As we have previously reported, a cooperative luminescence effect observed for Er-doped t-$BiVO_4$ would explain the *vis-NIR* photoactivity. In the case of co-doped $BiVO_4$ which exhibits pure tetragonal structure the photocatalytic enhancement cannot be associated to the presence of a phase heterostructure. Furthermore, the reaction rate for this system is notably higher with respect to single doped systems. Lower photoactivities reported in the literature for t-$BiVO_4$ was explained considering the wider band gap for this phase. Thus, in our case the exalted photoluminescence observed in Raman spectra for

Er^{3+},Y^{3+}-$BiVO_4$ with respect to Er^{3+}-$BiVO_4$ upon illumination with 532 nm laser would point out the participation of such luminescence process in the overall mechanism. In summary, the notably enhanced photoactivity observed upon sun-like irradiation would be associated to a double cooperative mechanism. On one hand yttrium incorporation would affect to the conduction band position.[31] The participation of Y *4d* orbital in the conduction band hybridization would shift to a higher position with respect to the conduction band for m-$BiVO_4$. Thus, Y^{3+} would help to the improved photon efficiency, enhancing the *UV*-photoassisted process by increasing the electron-hole separation driving force. Secondly, the presence of erbium and the associated luminescence up-conversion process could improve the photoefficiency within the *vis-NIR* region by increasing the absorbed photons. Similar effect was already observed for Er^{3+} doped TiO_2, for which an up-conversion mechanism would be the responsible in part of the better photocatalytic behaviour under *vis-NIR* irradiation.[22,34]

The durability of the Er,Y-$BiVO_4$ system was evaluated through the recycling of the used catalyst (**Figure 7**). For each cycle, the catalyst was collected by filtration and washing. As it can be observed from consecutive degradation cycles, there was no apparent loss of photocatalytic activity across the four cycles performed. The diminution of photocatalytic activity was less than 2%. Therefore, it can be deduced that the Er,Y codoped $BiVO_4$ has good photostability and reusability which denotes its potential for industrial utilization.

Furthermore, in **Figure 8** it is shown the photocatalytic water oxidation activity of different $BiVO_4$ samples from an aqueous solution containing $AgNO_3$ as a sacrificial reagent under sunlight irradiation. In spite of that our starting m-$BiVO_4$ does not show the excellent photocatalytic performance as that reported in ref.10, O_2 evolution of our m-$BiVO_4$ is in the range of other reported bismuth vanadates.[35,36] Moreover, the O_2

evolution for different doped $BiVO_4$ catalyst plainly denotes a notably beneficial effect. In all cases, the O_2 evolution rates for these samples are markedly improved with respect to bare m- or t-$BiVO_4$ (**Table 3**). This trend is in accordance to the previous behaviour for *MB* photodegradation reaction above discussed. Moreover, the photocatalytic performance showed for Er^{3+},Y^{3+} co-doped $BiVO_4$ appears significantly enhanced with respect to single doped systems (425 $\mu mol \cdot h^{-1} \cdot g^{-1}$ vs. ca. 300 $\mu mol \cdot h^{-1} \cdot g^{-1}$ respectively). Then, the calculated reaction rate for co-doped system is 8 times higher with respect to the m-$BiVO_4$ reported in the present work. By observing the reaction rate for t-$BiVO_4$, this enhancement cannot be exclusively associated to the increase in surface area or higher UV adsorption. The occurrence of both lanthanide ion dopants leads to a synergetic effect that could be explained by considering their double role.

4. Conclusions.

We have obtained a highly active Er^{3+},Y^{3+}-$BiVO_4$ system exhibiting tetragonal structure. The hydrothermal synthesis leads to homogeneous $BiVO_4$ rice-like nanoparticles of ca. 200-400 nm length size. From the chemical and structural analysis the incorporation of lanthanide dopant ions into $BiVO_4$ structure has be stated. The photocatalytic activities for the *Methylene Blue* degradation and O_2 evolution reactions clearly evidence the beneficial effect of doping. Moreover, it is worthy to note that tetragonal phase co-doped $BiVO_4$ shows a significantly higher photoactivity with respect to bare m-$BiVO_4$ and t-$BiVO_4$. From the photocatalytic experiments we tentatively propose a double mechanism which could explain the improved photoactivities in doped systems. On one hand, the presence of Er^{3+} and Y^{3+} improved the electronic charge separation process, enhancing the *UV*-photoassisted process. This mechanism is consistent with a classical doping conception since we used $BiVO_4$ as

host material. Moreover, it can be evidenced a small contribution of *vis-NIR* photons to UV-active tetragonal co-doped $BiVO_4$ in the overall mechanism probably due to an energy transfer process from erbium ions. As a result, the Er^{3+},Y^{3+} co-doped $BiVO_4$ shows a notably improved photoactivity with respect to m-$BiVO_4$. By handling the band and photon absorption features we propose a highly active material for O_2 evolution from water splitting reaction.

Acknowledgements.

The financial support by projects *P09-FQM-4570* and *ENE2011-24412* is fully acknowledged. S. Obregón Alfaro thanks CSIC for the concession of a JAE-Pre grant.

References.

1 D. Ravelli, D. Dondi, M. Fagnoni, A. Albini, *Chem. Soc. Rev.* **2009**, *38*, 1999-2011.

2 M. Pelaez, N.T. Nolan, S.C. Pillai, M.K. Seery, P. Falaras, A.G. Kontos, P.S.M. Dunlop, J.M.J. Hamilton, J.A. Byrne, K. O'Shea, M.H. Entezari, D.D. Dionysiou, *App. Catal. B: Environ.* **2012**, *125*, 331–349.

3 M. Maeda, K. Domen, *J. Phys. Chem. C* **2007**, *111*, 7851–7861.

4 A. Kubacka, M. Fernández-García, G. Colón, *Chem. Rev.* **2012**, *112*, 1555–1614.

5 A. Kudo, Y. Miseki, *Chem. Soc. Rev.* **2009**, *38*, 253–278.

6 K. Maeda, *J. Photochem. Photobiol. C: Photochem. Rev.* **2011**, *12*, 237–268.

7 K. Sayama, R. Yoshida, H. Kusama, K. Okabe, Y. Abe, H. Arakawa, *Chem. Phys. Lett.* **1997**, *277*, 387–391.

8 K. Maeda, *ACS Catal.*, **2013**, *3*, 1486–1503.

9 J. Yang, D. Wang, X. Zhou, C. Li, *Chem. Eur. J.* **2013**, *19*, 1320–132.

10 A. Kudo, K. Omori, H. Kato, *J. Am. Chem. Soc.* **1999**, *121*, 11459–11467.

11 Y. Park, K.J. McDonald, K.S. Choi, *Chem. Soc. Rev.* **2013**, *42*, 2321–2337.

12 D. Ke, T. Peng, L. Ma, P. Cai, K. Dai, *Inorg. Chem.* **2009**, *48*, 4685–4691.

13 H. Jiang, H. Dai, X. Meng, L. Zhang, J. Deng, Y. Liu, C.T. Au, *J. Environ. Sci.* 2**012**, *24*, 449–457.

14 L. Pan, X. Liu, Z. Sun, C.Q. Sun, *J. Mater. Chem. A* , **2013**, *1*, 8299–8326.

15 S. Tokunaga, H. Kato, A. Kudo. A. *Chem. Mater.* **2001**, *13*, 4624–4628.

16 H.M. Zhang, J.B. Liu, H. Wang, W.X. Zhang, H. Yan, *J. Nanopart. Res.* **2008**, *10*, 767–774.

17 Y.K. Kho, W.Y. Teoh, A. Iwase, L. Mädler, A. Kudo, R. Amal, *ACS Appl. Mater. Interfaces*, **2011**, *3*, 1997–2004.

18 Z. Zhang, W. Wang, J. Xu, M Shang, J. Ren, S. Sun, *Catal. Comm.* **2011**, *13*, 31–34.

19 T. Zhou, J. Hu, J. Li, *Appl. Catal. B: Environ.* **2011**, *110*, 221–230.

20 Z.X. Li, F.B. Shi, T. Zhang, H.S. Wu, L.D. Sun, C.H. Yan, *Chem. Comm.* **2011**, *47*, 8109–8111.

21 R. Adhikari, G. Gyawali, S.H. Cho, R. Narro-García, T. Sekino, S.W. Lee, *J. Solid State Chem.* **2014**, *209*, 74–81.

22 S. Obregón, G. Colón, *Chem. Comm.* **2012**, *48*, 7865–7867.

23 S. Obregón, S.W. Lee, G. Colón, *Dalton Trans.* **2014**, *43*, 311.

24 S. Usai, S. Obregón, A.I. Becerro, G. Colón, *J. Phys Chem. C* **2013**, *117*, 24479−24484.

25 H. Fan, T. Jiang, H. Li, D. Wang, L. Wang, J. Zhai, D. He, P. Wang, T. Xie, *J. Phys. Chem. C* **2012**, *116*, 2425–2430.

26 R.D. Shannon, *Acta Cryst.* **1976**, *32*, 751–767.

27 S.R.M. Thalluri, C. Martínez-Suarez, A. Virga, N. Russo, G. Saracco, *Int. J. Chem. Engineer. Appl.* **2013**, *4*, 305–309.

28 J. Yu, A. Kudo, *Chem. Lett.* **2005**, *34*, 850–851.

29 C.C. Ting, S.Y. Chen, W.F. Hsieh, H.Y. Lee, *J. Appl. Phys.* **2001**, *90*, 5564–5569.

30 F.D. Hardcastle, I.E. Wachs, *J. Phys. Chem.* **1991**, *95*, 5031–5041.

31 H. Liu, J. Yuan, Z. Jiang, W. Shangguan, H. Einaga, Y. Teraoka, *J. Mater. Chem.*, **2011**, *21*, 16535–16543.

32 J. Yu, A. Kudo, *Adv. Funct. Mater.* **2006**, *16*, 2163–2169.

33 S. Obregón, A. Caballero, G. Colón, *Appl. Catal. B: Environ.* **2012**, *117– 118*, 59–66.

34 S. Obregón, A. Kubacka, M. Fernández-García, G. Colón, *J. Catal.* **2013**, *299*, 298–306.

35 W. Yao, J. Ye, *Chem. Phys. Lett.* **2008**, *450*, 370–374.

36 J. Yu, Y. Zhang, A. Kudo, *J Solid State Chem.* **2009**, *182*, 223–228.

Tables.

Table 1. Structural characterization for $BiVO_4$ and Er^{3+},Y^{3+} doped catalysts.

Samples	monoclinic			tetragonal		Microstrain		Monoclinic Cell volume ($Å^3$)	Tetragonal Cell volume ($Å^3$)	Tetragonal %
	a	*b*	*c*	*a=b*	*c*	Monoclinic	Tetragonal			
m-$BiVO_4$	5.2015	5.1008	11.7198	---	---	0.005	---	310.95	---	0
t-$BiVO_4$	---	---	---	7.3047	6.4613	---	0.040	---	344.6	95
Er^{3+}-$BiVO_4$	5.2220	5.1031	11.7080	7.2969	6.4533	0.049	0.068	312.00	344.6	55
Y^{3+}-$BiVO_4$	5.2062	5.1007	11.7200	7.2976	6.4540	0.206	0.145	311.23	343.9	68
Er^{3+},Y^{3+}-$BiVO_4$	---	---	---	7.2955	6.4535	---	0.153	---	343.8	100

Table 2. Structural features from Raman characterization for $BiVO_4$ and Er^{3+}, Y^{3+} doped catalysts.

Samples	Raman Frequency (cm^{-1})		Bond length V-O (Å)	
	monoclinic	tetragonal	monoclinic	tetragonal
m-$BiVO_4$	824.99	---	1.6966	---
t-$BiVO_4$	---	850.15	---	1.6809
Er^{3+}-$BiVO_4$	825.13	850.02	1.6965	1.6810
Y^{3+}-$BiVO_4$	825.88	851.63	1.6960	1.6800
Er^{3+},Y^{3+}-$BiVO_4$	---	---	---	1.6803

* The positions of the most intense bands near 825 cm^{-1} and 850 cm^{-1} were determined by the fitting to the Lorentzian peak function.

Table 3. Surface, electronic and photocatalytic characterization for $BiVO_4$ and Er^{3+},Y^{3+} doped catalysts.

Samples	BET (m^2/g)	Band gap (eV)		Ln^{3+} content		*MB* degradation Reaction rate ($\cdot 10^{-4}$ s^{-1})		O_2 evolution ($\mu mol \cdot h^{-1} \cdot g^{-1}$)
		monoclinic	tetragonal	Er^{3+}/Bi^{3+}	Y^{3+}/Bi^{3+}	*UV-vis-NIR*	*Vis-NIR*	
m-$BiVO_4$	<1	2.39	---	---	---	1.26	0.458	53
t-$BiVO_4$	5	---	2.86	---	---	0.99	0.061	37
Er^{3+}-$BiVO_4$	2	2.39	2.75	0.006	---	5.10	0.149	320
Y^{3+}-$BiVO_4$	3	2.38	2.77	---	0.033	4.03	0.141	285
Er^{3+},Y^{3+}-$BiVO_4$	5	---	2.83	0.006	0.029	6.55	0.205	425

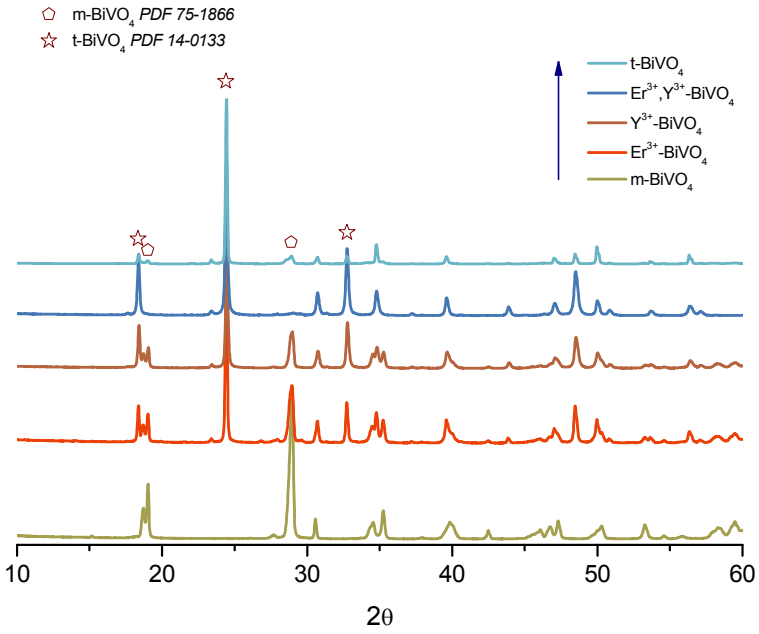

FIGURE 1. XRD patterns for different $BiVO_4$ catalysts obtained by hydrothermal synthesis at 140ºC for 20 h.

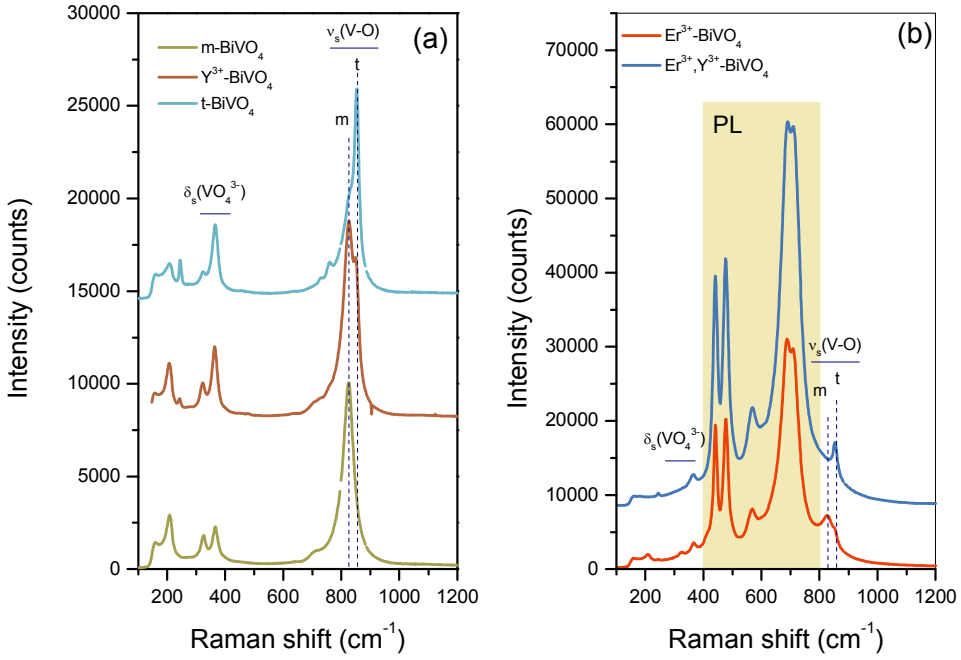

FIGURE 2. Raman spectra obtained upon green laser (532 nm) excitation for: a) undoped m- and t-$BiVO_4$ and Y^{3+}-$BiVO_4$ systems; b) Er^{3+}-$BiVO_4$ and Er^{3+},Y^{3+}-$BiVO_4$ systems (PL denotes the photoluminescence bands corresponding to Er^{3+} presence).

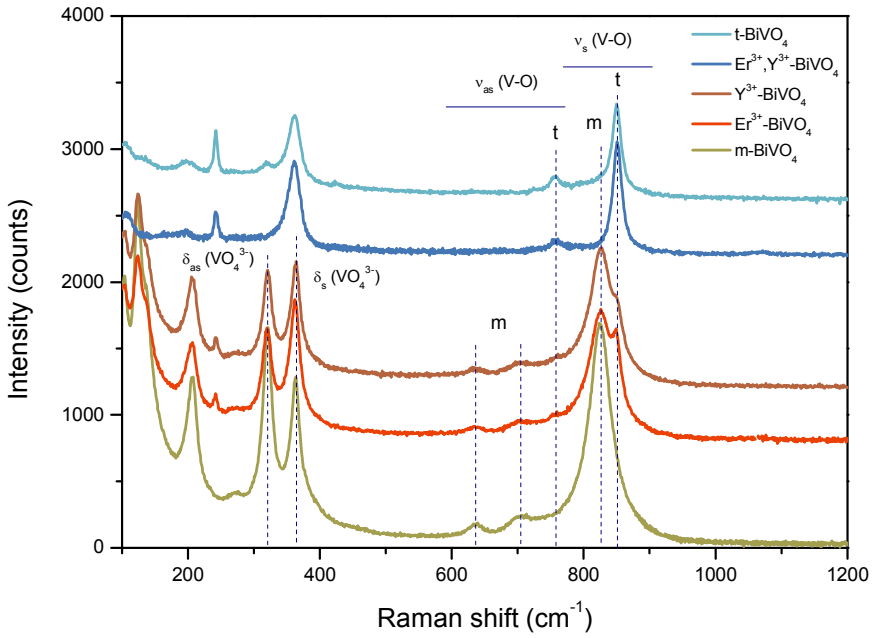

FIGURE 3. Raman spectra for different $BiVO_4$ catalysts obtained upon red laser (780 nm) excitation.

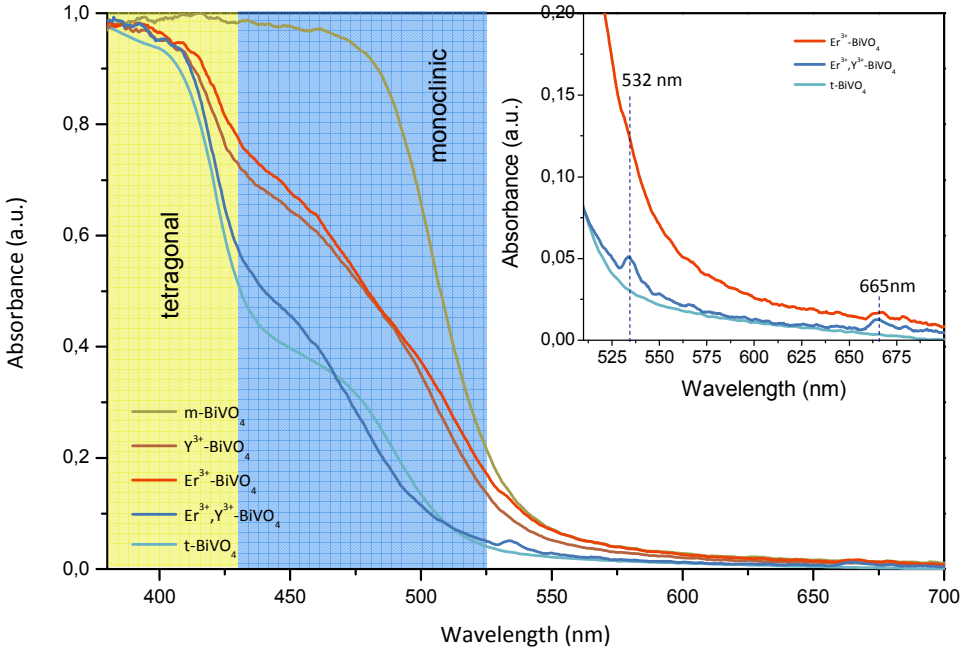

FIGURE 4. Evolution of diffuse reflectance spectra for different bare and doped $BiVO_4$ catalysts obtained by hydrothermal synthesis at 140ºC for 20 h (inset: t-$BiVO_4$ and Er-doped systems are compared).

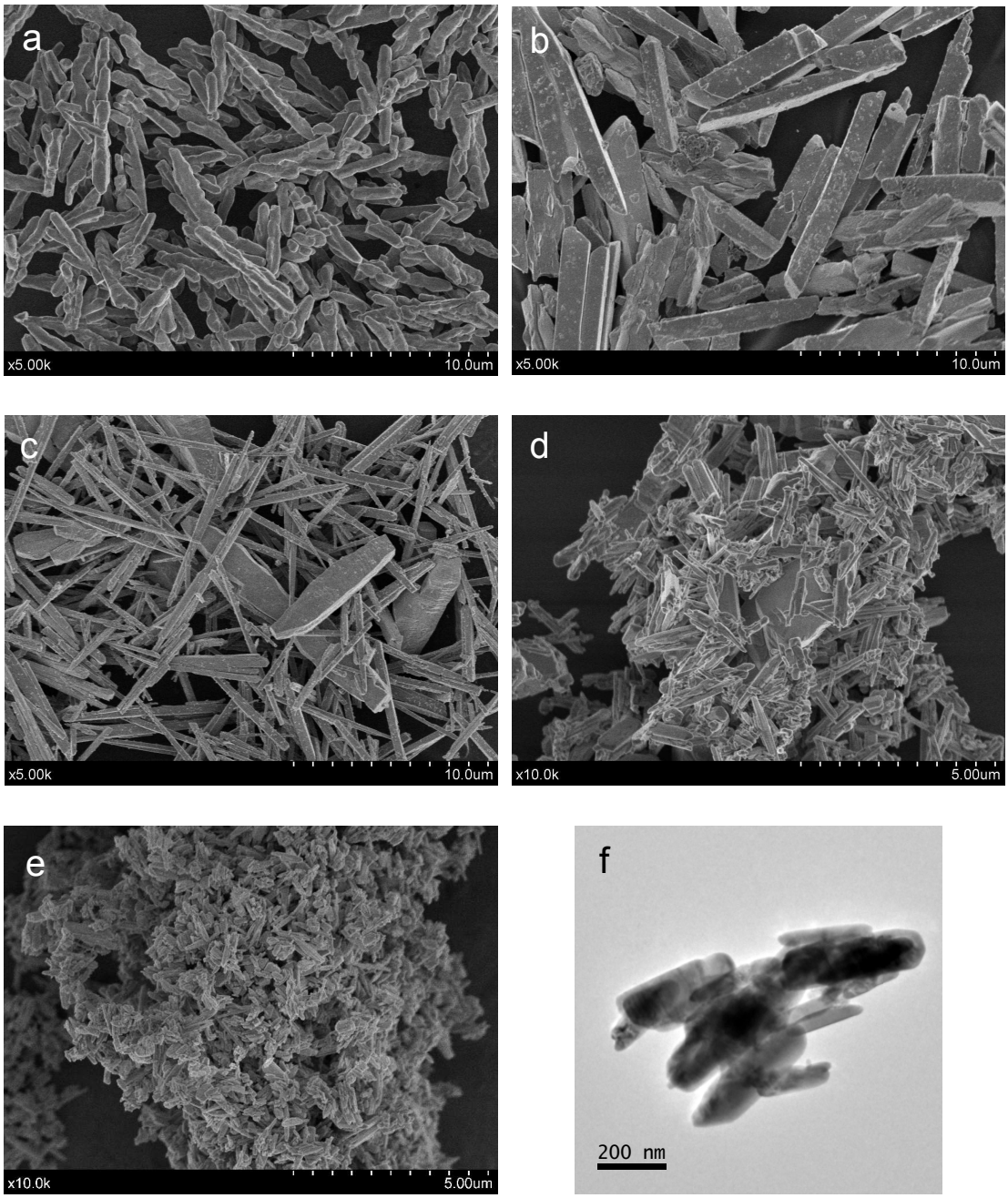

FIGURE 5. FESEM images of different $BiVO_4$ systems: a) bare m-$BiVO_4$; b) bare t-$BiVO_4$; c) Er^{3+}-$BiVO_4$; d) Y^{3+}-$BiVO_4$; e) Er^{3+},Y^{3+} co-doped $BiVO_4$; f) TEM image of Er^{3+},Y^{3+} co-doped $BiVO_4$.

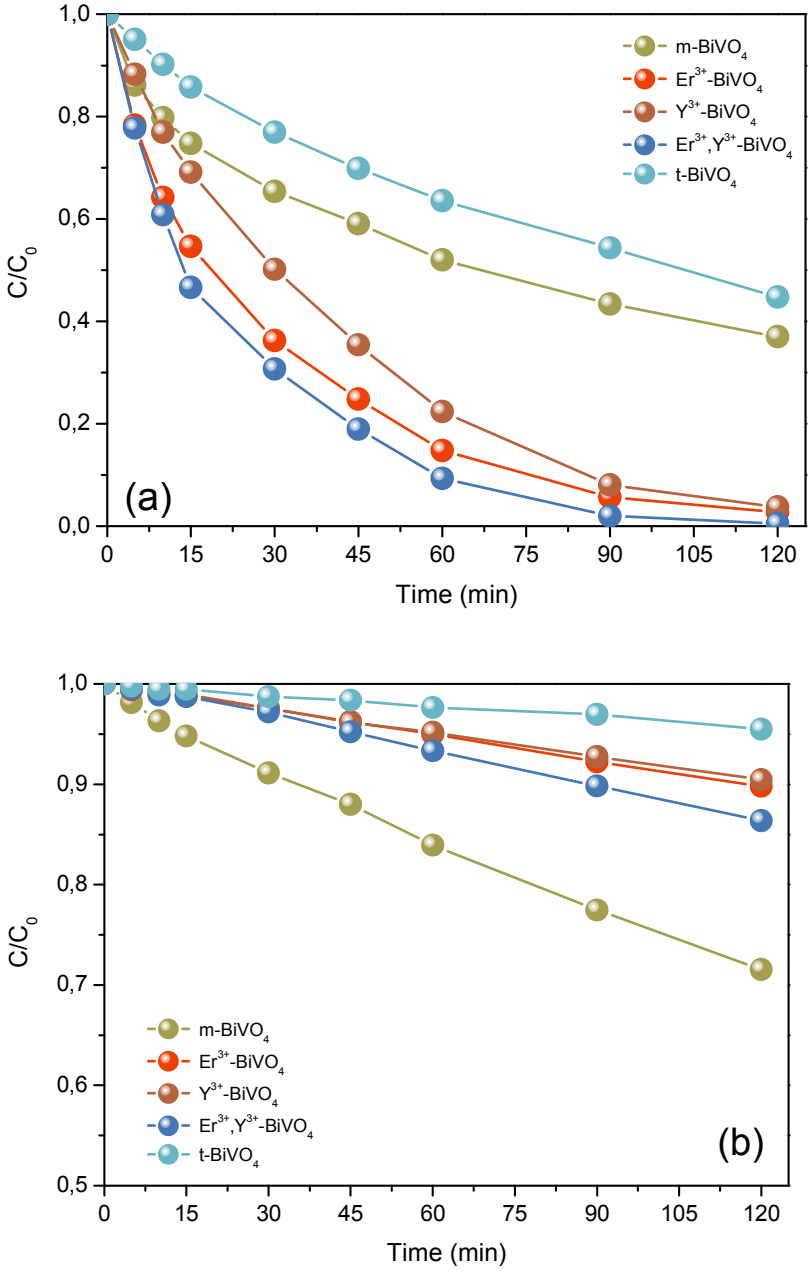

FIGURE 6. Evolution of *MB* with photodegradation time for different for $BiVO_4$ catalysts. a) upon *UV-vis-NIR* irradiation; b) Evolution of *MB* concentration upon *vis-NIR* irradiation

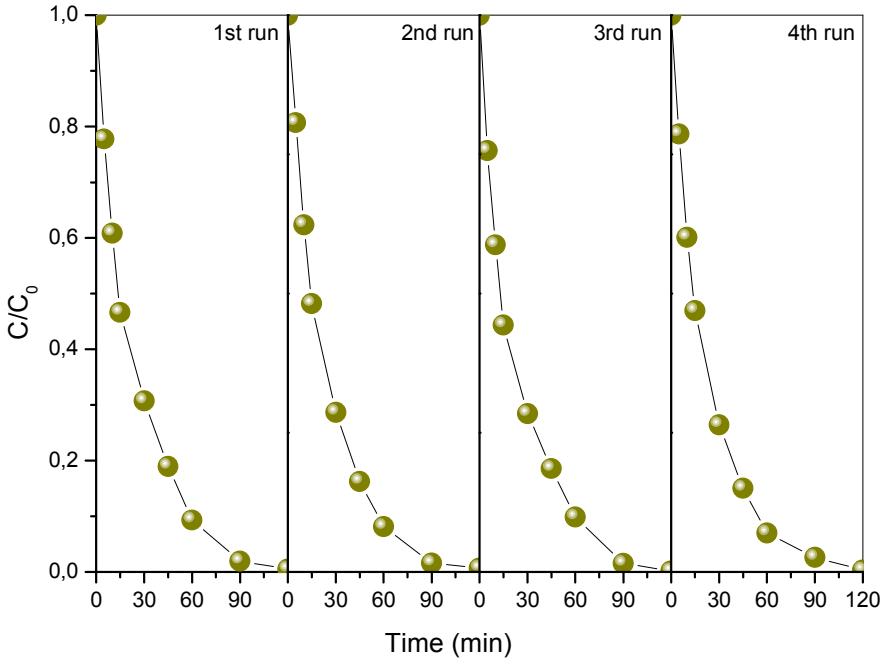

FIGURE 7. Reusability properties of the Er^{3+},Y^{3+}-$BiVO_4$ system for *MB* degradation reaction.

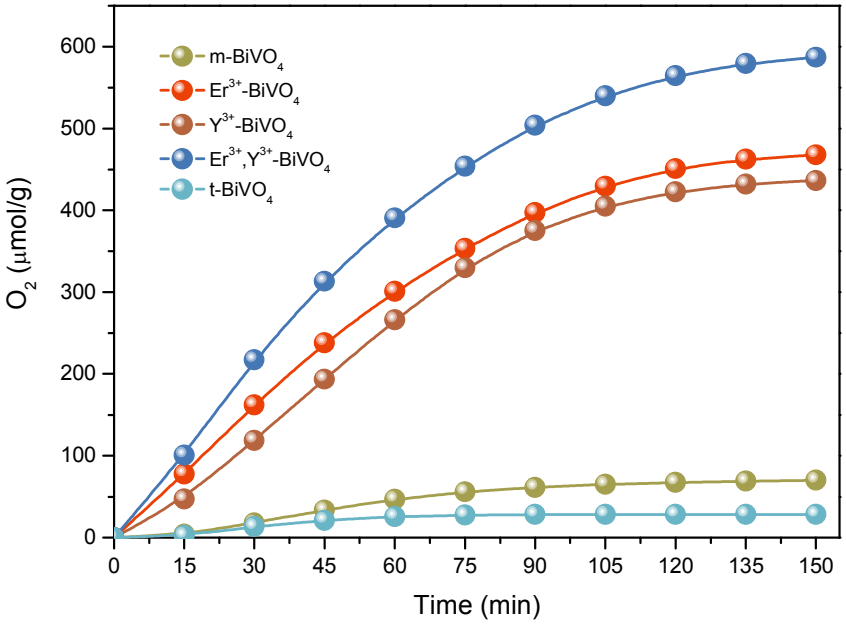

FIGURE 8. Photocatalytic O_2 evolution for different $BiVO_4$ samples from aqueous $AgNO_3$ solutions (0.02 $mol \cdot L^{-1}$) as a function of the irradiation time.